RSC Advances

PAPER

View Article Online
View Journal | View Issue

Cite this: *RSC Adv.*, 2022, **12**, 18224

Efficient Xe selective separation from Xe/Kr/N_2 mixtures over a microporous CALF-20 framework†

Yi Wei,[a] Fengshi Qi,[a] Yunhe Li,[a] Xiubo Min,[a] Qi Wang,[a] Jiangliang Hu*[b] and Tianjun Sun *[a]

Received 1st May 2022
Accepted 15th June 2022

DOI: 10.1039/d2ra02768b

rsc.li/rsc-advances

Capture and separation of xenon and krypton by adsorption are particularly important issues at room temperature in both industry and environmental security. Herein, hydrophobic zinc-based frameworks (CALF-20) were synthesized to separate mixtures of Xe, Kr and N_2, and adsorptive properties and stability of as-prepared samples were investigated in detail. CALF-20 with the 1,2,4-triazole and oxalate as the ligand and Zn metal centers showed a surface area of 442 m^2 g^{-1} and average pore size of 6–7 Å, and exhibited excellent stability in a high-temperature acidic solution. The single and binary adsorption datum represented that CALF-20 has a high Xe uptake of 2.45 mmol g^{-1} and Xe/Kr selectivity of 13.2, as well as high Xe/N_2 selectivity of 62 at 298 K and 1.0 bar. The initial adsorption heat and Henry's constant of Xe on the CALF-20 were determined to be 31.7 kJ mol^{-1} and 21.77 mmol g^{-1} bar^{-1} by isotherms, indicating a suitable affinity for Xe capture and Xe/Kr separation. In addition, simulation results indicated that the simulated adsorption isotherms and adsorption heats are well-matched with experimental results, and the adsorption affinity from the C–H groups of 1,2,4-trizole ring for Xe is significantly stronger than that for Kr.

1 Introduction

The capture and separation of Xe and Kr by adsorption are of great importance in the field of industry and environmental security.[1] In general, Xe and Kr have been widely used in lighting, electronics, lasers, medical devices, anesthetics, and propellants in ion propulsion engines, because of their specific properties including the high density, low chemical reactivity and solubility, very low boiling and conductivity.[1,2] Meanwhile, trace Xe and Kr capture was a critical problem in the monitoring of radioisotopes worldwide and removing radioactive contamination of nuclear waste.[3,4] As we all know, heavier noble gases all possess very low abundances at the ppmv level in air and industrial off-gases, making them difficult to capture and separate directly from air. Conventionally, cryogenic distillation was a common method to concentrate the Xe and Kr from air and the selective capture of radioactive noble gases from spent nuclear fuel.[5] As we all know, cryogenic distillation is a typical energy- and capital-intensive method for producing these heavier noble gases, which greatly limits commercial applications.[6] Therefore, looking for a feasible and high-efficiency method for heavier noble gas capture and purification has attracted much attention in the field of gas separation due to the fast-growing demand for Xe and Kr in the next few decades. Alternatively, extensive research has been done to adopt physisorption with suitable absorbents to capture and separate Xe and Kr at or near room temperature for the advantages of low cost, high efficiency, and reliability.[1,7]

Currently, activated carbon,[8–10] zeolites,[11–14] and metal–organic frameworks (MOFs)[15,16] have drawn great attention for the high-efficient separation of Xe and Kr by adsorption. However, there is always a major challenge to efficiently capture the trace noble gases from the gas mixture because of their chemical inertness and small size difference with nitrogen (kinetic diameter: Kr, 3.65 Å; N_2, 3.84 Å; Xe, 4.04 Å).[17] Precisely controlling pore characteristics is the primary method that needs to be solved urgently for achieving both high adsorption selectivity and high capacity of Xe and Kr.[18] Among the above-mentioned adsorbents, metal–organic frameworks have been considered to be a better adsorbent since their large surface areas, highly ordered pores, and fine-tuned properties by altering the building blocks.[1,19] Mueller *et al.* first reported that IRMOF-1 had a good Xe/Kr separation property at room temperature,[20] but Thallapaly *et al.* found that the xenon adsorption capacity of MOF-5 was only half that of activated carbon (*ca.* 27 wt%) at normal pressure and temperature.[21] Lee *et al.* subsequently revealed that the xenon uptake and Xe/Kr selectivity of UIO-66 at 1 bar and 303 K can reach 1.58 mmol g^{-1} and 7.15, respectively, which is superior to that of Cr-Mil-101 and Fe-Mil-100, and is better than traditional activated

---

[a] *Marine Engineering College, Dalian Maritime University, Dalian 116026, China. E-mail: suntianjun@dlmu.edu.cn*

[b] *State Key Laboratory of Clean and Efficient Coal Utilization, Taiyuan University of Technology, Taiyuan 030024, China. E-mail: hujiangliang@tyut.edu.cn*

† Electronic supplementary information (ESI) available. See https://doi.org/10.1039/d2ra02768b

carbon in Xe/Kr selectivity.[22] Wall effect of ultra-micropores is known as a significant boost factor for the selective adsorption dominated by the polarization of gas molecules, and Wang first confirmed that metal formates with 5 Å pores possessed a good xenon uptake of 2 mmol g^{-1} and excellent Xe/Kr selectivity of 12 at room temperature.[23] Banerjee *et al.* studied systematically the adsorption of Kr and Xe in ultra-microporous MOFs, and found that the Xe/Kr separation selectivity of SBMF-1 (4.5 Å) reached up to 16 whereas the Xe/Kr selectivity of Crofour-1-Ni with pore size near the kinetic diameter of xenon was as high as 26 at room temperature and ambient pressure.[18,24] Xiong and Wang also investigated the xenon adsorption behaviors on ultra-microporous MOFs deeply, and reported that Zn-$(tmz)_2$ (4.3 Å), MOF-Cu-H (4–6 Å) and $Zn(ox)_{0.5}(trz)$ (4 Å) all had good adsorption properties that the xenon uptakes were above 2.5 mmol g^{-1} and Xe/Kr selectivity was up to 15.5 at 298 K and 1 bar.[25–27] The latest research found that the Xe/Kr adsorption selectivity of PAF-45S with a pore size of 5.2 Å was about 16.7,[28] while the Co-squarate frameworks with 4 Å pores and NbOFFIVE-2-Cu-i with 5 Å pores were as high as 54.1 and 43, respectively.[29,30] More importantly, the Co-squarate framework is especially applicable for trace xenon capture from air owing to the high Henry constant of 192 mmol g^{-1} bar^{-1}. Moreover, the induced force (static dipole polarizability or Debye force) from the special sites with the strong polarity of frameworks can also improve the noble gas adsorption,[31] such as HKUST-1, MOF-74-M, MOF-505, PCN-14 and NOTT, *etc.* For example, the xenon uptakes of HKUST-1 and Ni-MOF-74 with open metal sites could achieve 3.2 mmol g^{-1} and 4.23 mmol g^{-1} at room temperature and ambient pressure, which was about twice that of IRMOF-1.[20,21,32] Perry *et al.* studied the xenon adsorption performance of considerable MOFs with open metal sites, and then found that xenon adsorption capacities on Co-MOF-74, NOTT100 and PCN14 can reach above 6.1 mmol g^{-1}, 6.1 mmol g^{-1} and 7.1 mmol g^{-1} at 298 K and 1 bar, which are far ahead of all other adsorbents.[33] In addition, the Xe and Kr adsorption can be hindered by polar gases in many cases, especially in the gas stream containing H_2O and CO_2,[34] and the excellent tunability of surface property provides the possibility for MOFs to eliminate the competition of H_2O and CO_2.[35] In a word, MOFs have many special advantages in the adsorption of Xe and Ke because of their higher surface area, channel uniformity, and variable surface properties, however, the developments of high-efficient MOFs with good stability and scalability of the synthesis to overcome the limitation in cost control, are still important for the capture/separation of trace noble gases in near future.

In this work, zinc-based MOFs (CALF-20) were prepared in a facile hydrothermal synthesis from two different humidity-resistance ligands, the 1,2,4-triazolate and the oxalate.[37] The structural, durable and adsorptive properties of CALF-20 were characterized and evaluated by XRD, FT-IR, TG, liquid-nitrogen adsorption–desorption isotherms, single-gas sorption isotherms and binary breakthrough experiments. The obtained CALF-20 with a pore size of 6–7 Å determined from Ar isotherm, showed a Xe uptake and Xe/Kr selectivity as high as 2.54 mmol g^{-1} and 13.2 respectively, and the adsorption properties of Xe and Kr in the as-prepared CALF-20 were mainly discussed under different conditions. Moreover, GCMC simulation was employed to investigate the adsorption behavior in CALF-20 and revealed the polarization from C–H groups dominates the selective adsorption of Xe and Kr.

2 Experimental

2.1 Synthesis method

The CALF-20 frameworks were prepared in our laboratory according to the modus operandi reported previously.[36,37] In a typical process, zinc oxalate dihydrate (8.0 g, $C_2O_4Zn\cdot 2H_2O$, 99%) and 1,2,4-triazole (5.0 g, $C_2H_3N_3$, 99%) were dissolved in 70 mL methanol with continuous stirring. After an hour's stirring, the mixtures were injected into a Teflon-lined autoclave, which were heated at 453 K for 48 h. Subsequently, the products were naturally cooled from 453 K to room temperature, and the white precipitates were filtered from the growth solution and washed thoroughly with methanol. The obtained solids were dried in the open air at room temperature for 12 h, and defined as CALF-20-Raw. And then, the CALF-20-Raw samples were activated under vacuum at 333–373 K as adsorbents, and defined as CALF-20.

Afterwards, the CALF-20 sample was placed in the moist air (80% RH) to absorb H_2O molecules for 24 h and activated again under the above-mentioned condition, and the obtained samples were labeled as CALF-20-M and CALF-20-MA, respectively. In addition, the CALF-20 samples were also treated for 2 h at room temperature in 10 wt% water–methanol solution, 10 wt% ammonia (28%)–methanol solution, and 10 wt% formic acid (CH_2O_2, 88%)–methanol solution, and the obtaining samples were labeled as CALF-20-W, CALF-20-B, and CALF-20-A, respectively.

2.2 Material characterization

Powder X-ray diffraction (PXRD) patterns of all obtained samples were recorded in the 2θ range of 5–40° on an X-ray diffractometer (X-Pert PRO, PANalytical) at 40 kV, 40 mA with Cu-Kα radiation ($\lambda = 0.15406$ nm). Thermogravimetric analyses (TGA) were performed on a TA analyzer (Labsys Evo, Setaram) under air atmosphere, in which the TG profiles were collected from 50 to 800 °C at a rate of 10 °C min^{-1}. Fourier transform infrared (FTIR) spectra of all samples were detected on a Nicolet iS50 Fourier transform infrared spectrometer. The texture properties were measured by Argon adsorption at 87 K with the Autosorb iQ physical adsorption instrument (Quantachrome Instruments, Boynton Beach, Florida, USA), and the characterization details were shown in the ESI S1.†

2.3 Gas adsorption measurements

Adsorption properties of as-prepared MOFs were characterized by Xe (99.99%), Kr (99.99%) and N_2 (99.99%) isotherms in the pressure range of 0–100 kPa at 298 K, which was conducted on a volumetric gas adsorption instrument Autosorb iQ. The selectivities for different mixtures were calculated by Henry's law constants and ideal adsorbed solution theory (IAST) respectively, and experimental heats of adsorption (Qst) of Xe, Kr and N_2 were also estimated by Clausius–Clapeyron relation from measured gas adsorption isotherms. The calculation details of Henry's law constants, Henry selectivity, IAST selectivity, and Qst from isotherms were described in ESI S2.† The breakthrough experiments of Xe/Kr and Xe/Kr/N_2 mixtures were all carried out at 298 K and 1 bar on a home-made setup with a programmable control system,[39] in which the composition of the gas outlet was detected by online mass spectrometry (Pfeiffer Vacuum OmniStar GSD 320, Germany).

2.4 Simulation methods

The crystallographic information file (2084733.cif) of CALF-20 was taken from the Cambridge Structural Database (CSD). The coordinates of all atoms in the frameworks were optimized by DFT calculations with the VASP program (Vienna *Ab initio* Simulation Package), and further geometry optimizations were conducted for obtaining the low-energy structures by the Forcite module in Materials Studio, as shown in the ESI S3.†[38,40] The accuracy of the crystal structure model was confirmed by comparing the experimental XRD pattern with the XRD pattern simulated by the Reflex module. Adsorptions of Xe, Kr and N_2 on CALF-20 were carried out by using the Grand Canonical Monte Carlo (GCMC) method as implemented in the RASPA simulation code, and the simulation details were presented in the ESI S3.†

3 Results and discussion

3.1 Structure characterization

CALF-20 framework, with empirical formula $C_3H_2N_3O_2Zn\ 0.396(C_2H_6O)$, was synthesized according to a reported procedure.[36,37] As shown in previous work, CALF-20 possesses a 3D network with a $P2_1/c$ space group in the monoclinic system, which is constructed by layers of 1,2,4-triazolate-bridged zinc(II) ions and pillars of oxalate ions. In the framework, each Zn(II) atom is ligated by three nitrogen atoms from two distinct triazole ligands (the 1,2 positions of the triazolate bridge Zn dimers, and the 4-position of the next dimer) and two oxygen atoms from the chelating oxalate group. So, the internal cavity of the CALF-20 framework has a suitable size to hold a single xenon atom. Fig. 1a showed the typical diffraction patterns of the as-synthesized and activated powders of this Zn-MOF with mixed-ligands of triazolate and oxalate, revealing that CALF-20-Raw has the same crystal phase as the reported datum in 2014 and 2021.[36,37] The characteristic peaks at 11.0°, 13.9°, and 14.4° should be assigned to the (100), (011), and (110) diffractions of the CALF-20 framework. The typical peaks of the activated sample that the guest molecules in the cavities were decanted, were also in good agreement with the diffractions of CALF-20, which is different from the diffractions of $Zn(ox)_{0.5}(trz)$ in ref. 27.[27,36]

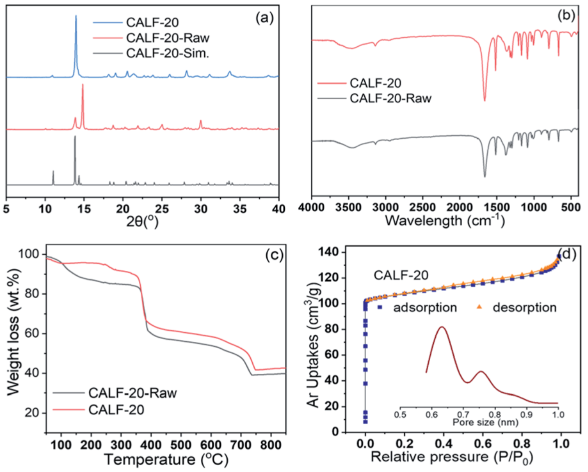

Fig. 1 (a) XRD patterns, (b) FT-IR spectra, and (c) TG curves of as-prepared CALF-20 frameworks; (d) Ar adsorption–desorption isotherms of CALF-20 framework at 87 K and (inset) PSD plot calculated by the NLDFT method.

FT-IR spectroscopy was adopted to measure the surface functional groups and the existence of ligands in the CALF-20 frameworks. As shown in Fig. 1b, the IR spectra of the CALF-20 before and after activation exhibit the same feature in the region of 400–1700 cm^{-1}. The analysis showed that the absorption peaks located at 1663 cm^{-1}, 1370 cm^{-1}, 1298 cm^{-1}, and 1167 cm^{-1} should be related to the stretching vibration of C═O, O═C–O, C–O, and C–C in the oxalate ligand, while the bands at 797 cm^{-1} and 495 cm^{-1} can be attributed to the bending vibration of O═C–O and the fingerprint peak of O–Zn related to oxalate. In addition, the absorption bands at 1663 cm^{-1}, 1517 cm^{-1}, 1323 cm^{-1}, 1207 cm^{-1}, and 1088 cm^{-1} should be ascribed to the stretching vibrational mode of C═N, the skeleton of triazole, C–N, N–N, and C–H in 1,2,4-triazole, and 900 cm^{-1}, 667 cm^{-1}, and 424 cm^{-1} are relevant to the bending vibrational modes of triazole ring and the fingerprint peaks of N–C═N and N–M in 1,2,4-triazole. To examine the stability of the CALF-20 frameworks, thermal gravimetric analysis experiments were carried out, as shown in Fig. 1c. The TG profile revealed the weight losses of 3.12 wt% and 2.47 wt% for CALF-20-Raw and CALF-20 samples in the temperature range of 50–100 °C, which should be caused by the release of free water molecules. When the temperature increased to 300 °C, the weight losses were about 10.91 wt% and 3.79 wt% for CALF-20-Raw and CALF-20, which should be related to the decomposition of some occluded 1,2,4-triazole (260 °C) and oxalate acid (189.5 °C) in samples, revealing there are much more occluded ligands in the CALF-20-Raw. After that, the biggest weight loss of *ca.* 45% started from 350 °C for both samples, which corresponds to two-stage collapse of the CALF-20 skeleton. In other words, the CALF-20 framework is still stable even at 350 °C, showing acceptable stability as an adsorbent. The porosity of the CALF-20 was evaluated by Ar adsorption at 87 K. As shown in Fig. 1d, the isotherm displayed type I sorption behavior, revealing that the CALF-20 framework is the microporous material. The BET surface area and total pore volume of CALF-20 were calculated to be 442 $m^2\ g^{-1}$ and 0.28 $cm^3\ g^{-1}$ from the isotherm, respectively. It should be noted the PSD plot shows two different micropores with pore sizes of 6.3 Å and 7.6 Å respectively, which is slightly bigger than the simulated pore size of CALF-20 in ref. 37.

3.2 Single gas adsorption measurements and adsorption selectivity

Single gas adsorption isotherms were firstly measured to appraise the separation performance of CALF-20 for Xe/Kr, Xe/N_2 and Kr/N_2 mixtures in the pressure range of 0–100 kPa at 288 K, 298 K, and 308 K, respectively. As shown in Fig. 2a, the adsorption capacities of CALF-20 at different temperatures all increased in the order of Xe > Kr > N_2, displaying that the larger polarizability is of great importance in the higher uptakes of Xe and Kr. The Xe uptake was up to 2.45 mmol g^{-1} at 1.0 bar and 298 K, while the Kr and N_2 capacities were about 1.12 mmol g^{-1} and 0.29 mmol g^{-1}. Notably, the Xe adsorption isotherm displayed a sharp increase at relative pressure (P/P_0) below 0.1, while the isotherms of Kr and N_2 on CALF-20 were approximately linear in the range of 0–1 bar, which revealed the interaction of Xe with CALF-20 is much stronger than that of Kr and N_2. These results showed that the Xe uptake is up to 1.26 mmol g^{-1}, but the Kr and N_2 uptakes are only 0.14 mmol g^{-1} and 0.033 mmol g^{-1} at 298 K and 0.1 bar, respectively. The experimental isosteric heats (Qst) of Xe, Kr and N_2 were estimated by the Clausius–Clapeyron equation from their adsorption isotherms at three different temperatures, as the above-mentioned method. Fig. 2b showed the adsorption heats of Xe, Kr and N_2 on CALF-20 were around 31.7 and 22.4, 16.9 kJ mol^{-1} at 298 K, respectively, revealing the stronger Xe interactions on CALF-20 over Kr and N_2. Actually, the adsorption heat of Xe has a certain advantage over many excellent MOFs, such as CROFOUR-1-Ni (37.4 kJ mol^{-1}), Al-CDC (34.9 kJ mol^{-1}), Co-Squarate (43.6 kJ mol^{-1}), SB-MOF-1 (35.0 kJ mol^{-1}), MOF-Cu-H (33.0 kJ mol^{-1}), and PAF-45S (31.0 kJ mol^{-1}), in which the stronger interactions would induce higher adsorption interaction and difficult desorption of Xe.

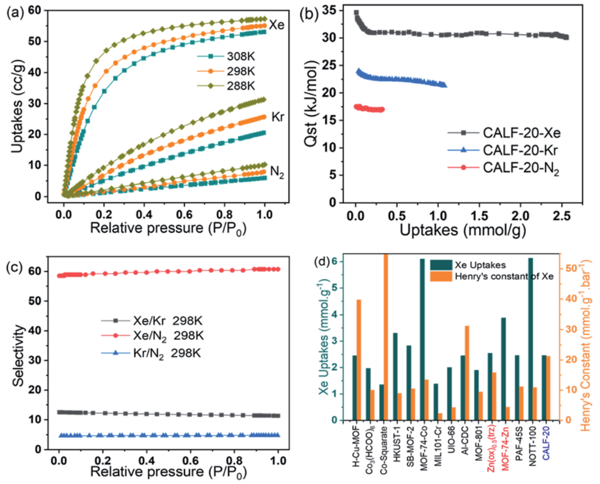

Fig. 2 (a) Adsorption isotherms and (b) adsorption heats of Xe, Kr and N_2 on CALF-20 framework, (c) IAST selectivity for equimolar Xe/Kr, Xe/N_2 and Kr/N_2 mixtures at 298 K and 1 bar, and (d) Xe uptakes and Henry's constants of Xe on some state-of-the-art adsorbents at 298 K and 1 bar.

The calculated Henry's selectivity and IAST selectivity from Xe, Kr and N_2 isotherms, can be used to evaluate the separation properties of Xe/Kr, Xe/N_2 and Kr/N_2 mixtures on CALF-20. Fig. 2c and Table S1† summarized the IAST selectivities for different mixtures and the fitting parameters of Henry's constants by eqn (S1)–(S5).† Firstly, Henry's constants of Xe, Kr, and N_2 were determined as 21.77, 1.65, and 0.35 mmol g^{-1} bar^{-1} from isotherms directly, which is obviously higher than the Xe Henry's constants of $Zn(ox)_{0.5}(trz)$ (15.8 mmol g^{-1} bar^{-1}).[27] Meanwhile, Henry's selectivities for binary mixtures of Xe/Kr, Xe/N_2 and Kr/N_2 can be evaluated as 13.2, 62.0, and 4.7 respectively. Fig. 2c displayed the selectivities for Xe/Kr, Xe/N_2 and Kr/N_2 mixtures obtained from IAST using an F–L model at 298 K, in the range of 11.4–12.5, 58.5–60.7, and 4.7–4.8 at different pressures, respectively. The IAST selectivities present excellent agreement with Henry's selectivity for the mixtures with Xe or Kr concentration over 1.0 vol%, but the IAST selectivities will depend heavily on the gas compositions in dilute Xe and Kr sources, especially at ppm-level.

As shown in Fig. 2c and Table S2,† the Xe/Kr selectivity in CALF-20 is comparable to that of top-ranking MOFs at 298 K and 1.0 bar, including Al-CDC (10.7), SB-MOF-2 (10.0), MOF-74-Co (10.4), $Zn(ox)_{0.5}(trz)$ (12.5), $Co_3(HCOO)_6$ (8.7), MOF-801 (8.9), and HKUST-1 (8.4). Interestingly, Henry's constant of Xe on CALF-20 is only less than that of MOF-Cu-H (39.7 mmol g^{-1} bar^{-1}), Co-Squarate (192 mmol g^{-1} bar^{-1}) and Al-CDC (31.2 mmol g^{-1} bar^{-1}), indicating the CALF-20 possesses a suitable interaction for Xe capture and Xe/Kr separation, as shown in Fig. 2d. Moreover, the Xe uptake of CALF-20 is on the same level as those of famous MOFs at 298 K and 1.0 bar, except the MOFs with unsaturated metal sites such as MOF-74-Co (6.1 mmol g^{-1}), MOF-74-Zn (3.88 mmol g^{-1}), HKUST-1 (3.33 mmol g^{-1}) and NOTT (6.13 mmol g^{-1}). As we all know, both higher adsorption capacity and selectivity is the key metric for an excellent adsorbent, because the high selectivity can increase the concentration of production gas and high capacity can reduce the size of the adsorption bed for an adsorptive separation process with the same operating parameters. Importantly, the higher Henry's constant is most important for dilute Xe capture, because the stronger Xe–host interaction can enhance the trapping capability of trace molecular and present a higher Henry's constant. Obviously, the separation performance of CALF-20 has exceeded most of the MOFs reported for Xe capture and separation according to integrated evaluation criteria, which cover Xe uptake, Xe/Kr selectivity and Henry's constant of Xe.

3.3 Stability studies

From the application point of view, the stability of CALF-20 should be confirmed carefully under different conditions, such as heat, water, acid and base resistances, because the strong adsorptions of these contenders always result in intensive thermo-regeneration of adsorbents in the practical process. CALF-20 has shown excellent stability in moist and acid gas conditions, and the stabilities of CALF-20 under liquid water, acid solution, base solution and high temperature were verified

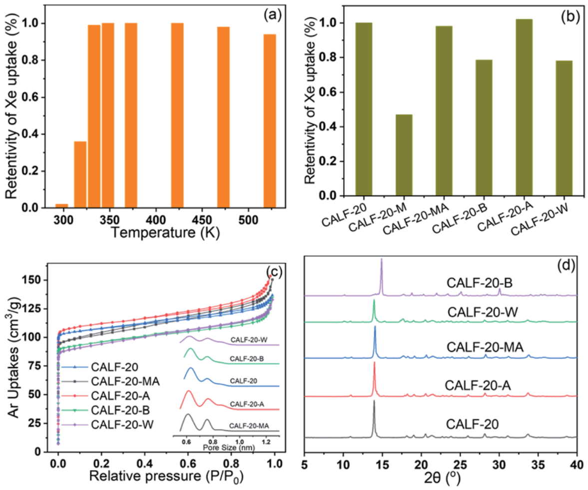

Fig. 3 (a) Comparison of Xe capacities at 298 K and 1 bar on CALF-20 frameworks activated at different temperatures, (b) retention rates of Xe capacities at 298 K and 1 bar on CALF-20 frameworks after the treatments with different solutions, (c) Ar adsorption isotherms at 87 K and (d) XRD patterns of CALF-20 frameworks treated by different solutions.

further in this work. Fig. 3a showed the Xe capacity of CALF-20 under different activation temperatures. Apparently, the CALF-20 was activated completely at 333 K and obtained the best Xe capacity at 298 K and 1 bar. CALF-20 retained a higher Xe capacity up to 473 K, and only lost 6% Xe capacity at 523 K, which presents excellent thermo-stability and is consistent with the TG results. As we all know, the dews could appear on the surfaces of porous materials under high humidity conditions (>80% RH), which has a significant negative effect on the Xe adsorption and can even destroy the framework of MOFs. As shown in Fig. 3b, the CALF-20 were treated in high humidity feedgas, water, acid and base solutions, and for investigating the stability. Clearly, the Xe capacity of CALF-20 decreased by 50% when it was exposed for 12 h in air with 80% RH (relative humidity), and recovered after being heated at 100 °C for 3 h under vacuum. Unfortunately, the retentions of Xe capacity on CALF-20 were about 78% and 79% after the treatment in the water and base solutions, and could not restore to the initial state by regeneration in the temperature range of 50–250 °C under vacuum, as the CALF-20-W and CALF-20-B samples shown in Fig. 3b. Similar to the results in the literature,[37] the adsorption capacity of Xe presented a slight increase after the treatment of CALF-20 using acid solutions, indicating the excellent acid resistance, as the CALF-20-A in Fig. 3b. The textural properties of CALF-20 treated under different conditions were shown in Fig. 3c. Obviously, the specific surface area of CALF-20-A showed a little increase, while other samples all dropped after treatments, especially the CALF-20-W/B samples. PSD profiles in the inset presented the same appearance that the pore volumes of CALF-20-B/W treated by water and base solution decline obviously, but the gaseous water and acid solution have no negative effects on the pore structures of CALF-20. PXRD, FTIR and TG were all performed to investigate the structural changes following treatment of the CALF-20, as shown in Fig. 3d, S1 and S2.† Specifically, the framework of CALF-20 exhibited high stability in the acid solution, gaseous and liquid water. And the diffraction peak of CALF-20-B was proven to be consistent with the characteristic peaks of CALF-20, except that the diffraction intensity of (110) increased and shifted to 15°, which is like a diffraction peak of CALF-20-Raw.

3.4 Breakthrough experiment

Dynamic breakthrough experiments were conducted to determine the separation performances of CALF-20 toward the binary Xe/Kr and ternary Xe/Kr/N_2 mixtures. Before the experiments, CALF-20 was activated in a helium flow at 373 K for 2 h. Fig. 4a showed the typical breakthrough curves of the Xe/Kr mixtures (50–50, 20–80, and 5–95 v/v%) in a packed column with granular CALF-20 at 1.0 bar and 298 K. For every breakthrough curve, Kr always eluted first, while Xe flowed through the packed column after a long time, suggesting Xe preferentially adsorbed on CALF-20 from these Xe/Kr mixtures. The big difference in residence times between Xe and Kr in the breakthrough process reveals CALF-20 is a high-efficiency adsorbent for separating Xe/Kr mixtures. It should be noted that there are always the classical roll-up peaks in the Kr breakthrough curves, indicating the Kr concentration at the elution gas significantly surpasses the feed concentration and increases sharply before the Xe breakthrough. This issue should come down to the partial desorption of the adsorbed Kr due to a thermal effect from the exothermic adsorption of Xe and the effect of competitive adsorption by Xe. For 50–50 v/v% Xe/Kr mixture, the breakthrough of Xe occurred at about 265 s which is later than that of Kr (about 60 s), showing the stronger interaction between Xe and CALF-20. The Xe working capacity and Xe/Kr selectivity were calculated to be 0.65 mmol mL^{-1} and 12.5 from the breakthrough curve of the 50–50 v/v% Xe/Kr mixture, which is in agreement with Henry's selectivity. Moreover, we have also investigated the effect of Xe concentration (20% and 5%) on the breakthrough performance of CALF-20, as shown in Fig. 4. With the decrease of Xe concentrations from 50% to 5%, Xe breaks from 265 to 460 s, enabling CALF-20 to be superiorly useful to purify the low-concentration Xe/Kr mixture. The breakthrough experiment of a ternary Xe/Kr/N_2 (5v : 45v : 50v) mixture showed a similar result, indicating the excellent performance for separating Xe from the low-concentration Xe/

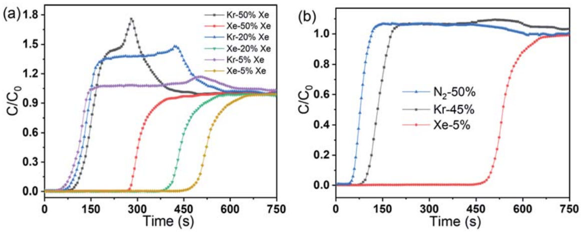

Fig. 4 Breakthrough curves of CALF-20 framework for the separation of (a) Xe/Kr mixtures with different Xe concentrations (50 vol%, 20 vol% and 5 vol%), and (b) Xe/Kr/N_2 mixture (5 : 45 : 50) at 298 K and 1 bar.

Kr/N_2 mixture, as shown in Fig. 4b. Based on these data, CALF-20 exhibits high Xe/Kr and Xe/N_2 selectivity, suggesting that it is one of the most promising adsorbents for Xe capture and separation.

3.5 Simulation studies

Simulated adsorption results of Xe, Kr and N_2 were obtained by the GCMC simulation method under pressure in the range of 0–100 kPa and 298 K. It can be learned from Fig. 5 that, the simulated isotherms of Xe, Kr and N_2 adsorption on CALF-20 approximately agreed with the measured adsorption isotherms, especially they presented very good accordance when the relative pressure (P/P_0) was below 0.3. However, the simulations slightly overpredicted the experimental uptakes after $P/P_0 > 0.4$, which should be attributed to a minor deviation of the force fields representing the adsorbent and adsorbates, as well as the drawbacks of the CALF-20 skeleton in the as-prepared samples. Based on the GCMC force field, the adsorption sites can be identified by the probability distributions of the Xe and Kr atoms within the CALF-20. The density distribution profiles of Xe and Kr in the cavity of CALF-20 at 0.1 bar and 298 K are presented in Fig. 6. It was evident that the adsorption behaviors of Xe and Kr are similar and all are adsorbed in the middle of the 1D channels, but the density distributions of Xe are significantly higher than that of Kr because the C–H groups in the specific cavity of CALF-20 deliver much stronger van der Waals forces to Xe. Furthermore, local views of the snapshots extracted showed that in the rhombus channels of CALF-20, Xe and Kr are similarly surrounded by H atoms of the 1,2,4-triazole rings, and the shortest and average distances of Xe–H are 3.447 and 4.456 Å, respectively. Due to the smaller atomic diameter and lower polarizability of Kr, the shortest distance (3.636 Å) and average distance (4.507 Å) of Kr–H are all longer than that of the Xe–H distance. The DFT calculations also showed that the adsorption heat of Xe (32.43 kJ mol^{-1}) on CALF-20 is much higher than that of Kr (23.42 kJ mol^{-1}), which coincides with the fact that the density distributions of Xe are stronger than Kr, and the experimental values of the isosteric heats. In a word, the simulated results from DFT and GCMC simulation illustrated that the abundant C–H groups were the specific adsorption sites of Xe adsorption.

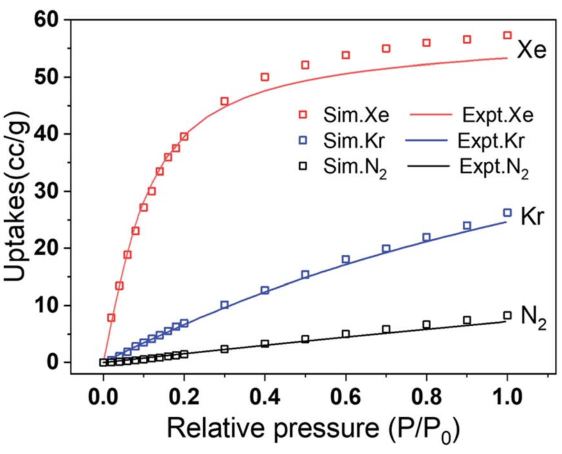

Fig. 5 Xe, Kr and N_2 adsorption isotherms of simulated (hollow blocks) and experimental (solid line) on CALF-20 at 298 K.

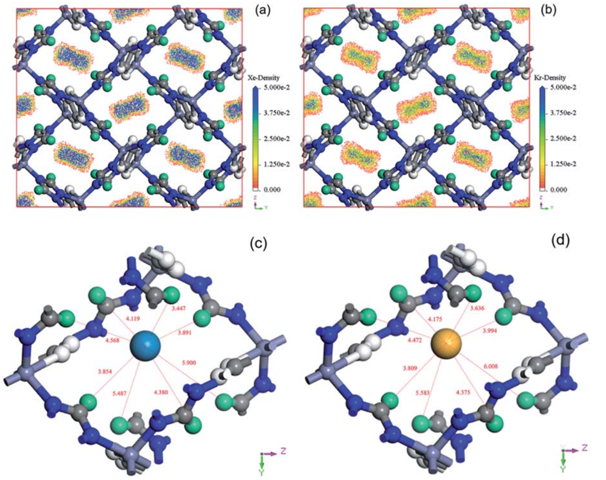

Fig. 6 Density distribution profiles of Xe (a) and Kr (b) on CALF-20 framework simulated at 0.1 bar and 298 K; local views of the snapshots extracted from GCMC simulations performed for Xe (c) and Kr (d) adsorption on CALF-20 frameworks. (The distance unit is Å, color mode: H, white; O, green; C, gray; N, blue; Zn, indigo blue; Xe, dark green; Kr, golden).

4 Conclusions

In this work, we have successfully synthesized a hydrophobic CALF-20 framework with a $P2_1/c$ space group in the monoclinic system by a simple hydrothermal method using 1,2,4-triazole and oxalate as the ligands. This intriguing material also showed prominent high-temperature, gaseous water and acid tolerance, and can retain the initial Xe uptake under vacuum recovery at 100 °C. Interestingly, CALF-20 presented a Xe capacity as high as 2.45 mmol g^{-1} at 298 K and 1.0 bar, especially the Xe uptake up to 1.26 mmol g^{-1} at 0.1 bar while the Kr and N_2 uptakes only *ca.* 0.14 mmol g^{-1} and 0.033 mmol g^{-1}, respectively. Importantly, CALF-20 exhibited good performances for Xe separation from Kr and N_2, such as Xe/Kr and Xe/N_2 selectivity up to 13.2 and 62 at 298 K and 1.0 bar, which was confirmed by the breakthrough experiments. The initial adsorption heat and Henry's constant of Xe on the CALF-20 MOF were determined to be 31.7 kJ mol^{-1} and 21.77 mmol g^{-1} bar^{-1} by isotherms and simulations, indicating a suitable affinity for the Xe capture and Xe/Kr separation which is the most important for dilute Xe capture and fast desorption of adsorbed Xe. In addition, the GCMC simulation indicated that the simulated and experimental isotherms show a good agreement at low relative pressures, and the C–H groups from the 1,2,4-triazole rings can deliver much stronger van der Waals interactions to Xe. As mentioned above, the separation performance of CALF-20 has exceeded most of the MOFs reported for Xe capture and separation according to integrated evaluation criteria, covering Xe uptake, Xe/Kr selectivity and Henry's constant of Xe.

Author contributions

Yi Wei: conceptualization, data curation, formal analysis, writing–original draft. Fengshi Qi: conceptualization, writing–original draft. Yunhe Li: data curation, writing–review & editing, software. Xiubo Min: writing–review & editing, data curation, software. Qi Wang: data curation. Jiangliang Hu: writing–review & editing, data curation. Tianjun Sun: conceptualization, formal analysis, project administration, writing–original draft, visualization.

Conflicts of interest

There are no conflicts to declare.

Acknowledgements

This work is financially supported by grants from the National Natural Science Foundation of China (No. 22078037, 52175378), CSC scholarship (No. 201906935005) and the Fundamental Research Funds for the Central Universities.

References

1 D. Banerjee, C. M. Simon, S. K. Elsaidi, M. Haranczyk and P. K. Thallapally, *Chem*, 2018, **4**, 466–494.
2 M. H. Mohamed, S. K. Elsaidi, T. Pham, K. A. Forrest, H. T. Schaef, A. Hogan, L. Wojtas, W. Q. Xu, B. Space, M. J. Zaworotko and P. K. Thallapally, *Angew. Chem., Int. Ed.*, 2016, **55**, 8285–8289.
3 N. R. Soelberg, T. G. Garn, M. R. Greenhalgh, J. D. Law, R. Jubin, D. M. Strachan and P. K. Thallapally, *Sci. Technol. Nucl. Install.*, 2013, **2013**, 1–12.
4 V. V. Prelovskii, N. M. Kzarinov, A. Yu. Donets, V. Yu. Popov, I. Yu. Popov and N. V. Skirda, *Instrum. Exp. Tech.*, 2007, **50**, 393–397.
5 F. G. Kerry, *Industrial Gas Handbook: Gas Separation and Purification*, CRC Press/Taylor & Francis Group, Florida, 2007.
6 R. Betzendhal, *The 2014 Rare Gases Market Report*, CryoGas International, 2014.
7 B. J. Sikora, C. E. Wilmer, M. L. Greenfield and R. Q. Snurr, *Chem. Sci.*, 2012, **3**, 2217–2223.
8 S. Zhong, Q. Wang and D. Cao, *Sci. Rep.*, 2016, **6**, 21295.
9 Y. J. Gong, Y. M. Tang, Z. H. Mao, X. N. Wu, Q. Liu, S. Hu, S. S. Xiong and X. L. Wang, *J. Mater. Chem. A*, 2018, **6**, 13696–13704.
10 F. Q. Chen, J. Q. Ding, K. Q. Guo, L. Yang, Z. G. Zhang, Q. W. Yang, Z. B. Bao, Y. He and Q. L. Ren, *Angew. Chem., Int. Ed.*, 2021, **60**, 2431–2438.
11 C. G. Saxton, A. Kruth, M. Castro, P. A. Wright and R. F. Howe, *Microporous Mesoporous Mater.*, 2010, **129**, 68–73.
12 L. Deliere, S. Topin, B. Coasne, J. Fontaine, S. D. Vito, C. D. Auwer, P. L. Solari, C. Daniel, Y. Schuurman and A. Farrusseng, *J. Phys. Chem. C*, 2014, **118**, 25032–25040.
13 L. Deliere, B. Coasne, S. Topin, C. Gréau, C. Moulin and D. Farrusseng, *Chem.–Eur. J.*, 2016, **22**, 9660–9666.
14 A. Monpezat, S. Topin, L. Deliere, D. Farrusseng and B. Coasne, *Ind. Eng. Chem. Res.*, 2019, **58**, 4560–4571.
15 S. K. Elsaidi, M. H. Mohamed, A. S. Helal, M. Galanek, T. Pham, S. Suepaul, B. Space, D. Hopkinson, P. K. Thallapally and J. Li, *Nat. Commun.*, 2020, **11**, 3103–3111.
16 S. H. Lou, F. Y. Ma, X. Wang, M. J. Yuan, L. H. Chen, S. K. Qiu, Q. Tang and S. Wang, *J. Radioanal. Nucl. Chem.*, 2020, **324**, 1275–1281.
17 J. R. Li, R. J. Kuppler and H. C. Zhou, *Chem. Soc. Rev.*, 2009, **38**, 1477–1504.
18 D. Banerjee, C. M. Simon, A. M. Plonka, R. K. Motkuri, J. Liu, X. Y. Chen, B. Smit, J. B. Parise, M. Haranczyk and P. K. Thallapally, *Nat. Commun.*, 2016, **7**, 11831.
19 C. M. Simon, R. Mercado, S. K. Schnell, B. Smit and M. Haranczyk, *Chem. Mater.*, 2015, **27**, 4459–4475.
20 U. Mueller, M. Schubert, F. Teich, H. Puetter, K. Schierle-Arndt and J. Pastre, *J. Mater. Chem.*, 2006, **16**, 626–636.
21 P. K. Thallapally, J. W. Grateb and R. K. Motkuria, *Chem. Commun.*, 2012, **48**, 347–349.
22 S. J. Lee, T. U. Yoon, A. R. Kim, S. Y. Kim, K. H. Cho, Y. K. Hwang, J. W. Yeon and Y. S. Bae, *J. Hazard. Mater.*, 2016, **320**, 513–520.
23 H. Wang, K. X. Yao, Z. J. Zhang, J. Jagiello, Q. H. Gong, Y. Han and J. Li, *Chem. Sci.*, 2014, **5**, 620–624.
24 M. H. Mohamed, S. K. Elsaidi, T. Pham, K. A. Forrest, H. T. Schaef, A. Hogan, L. Wojtas, W. Q. Xu, B. Space, M. J. Zaworotko and P. K. Thallapally, *Angew. Chem., Int. Ed.*, 2016, **55**, 8285–8289.
25 S. S. Xiong, Q. Liu, Q. Wang, W. Li, Y. M. Tang, X. L. Wang, S. Hu and B. L. Chen, *J. Mater. Chem. A*, 2015, **3**, 10747–10752.
26 S. S. Xiong, Y. J. Gong, S. L. Hu, X. N. Wu, W. Li, Y. B. He, B. L. Chen and X. L. Wang, *J. Mater. Chem. A*, 2018, **6**, 4752–4758.
27 L. Yu, S. S. Xiong, Y. H. Lin, L. Y. Li, J. J. Peng, W. Liu, X. X. Huang, H. Wang and J. Li, *Inorg. Chem.*, 2019, **58**, 15025–15028.
28 J. L. Li, L. Huang, X. Q. Zou, A. M. Zheng, H. Y. Li, H. Z. Rong and G. S. Zhu, *J. Mater. Chem. A*, 2018, **6**, 11163–11168.
29 L. Y. Li, L. D. Guo, Z. G. Zhang, Q. W. Yang, Y. W. Yang, Z. B. Bao, Q. L. Ren and J. Li, *J. Am. Chem. Soc.*, 2019, **141**, 9358–9364.
30 Q. J. Wang, T. Ke, L. F. Yang, Z. Q. Zhang, X. L. Cui, Z. B. Bao, Q. L. Ren, Q. W. Yang and H. B. Xing, *Angew. Chem., Int. Ed.*, 2020, **59**, 3423–3428.
31 J. N. Israelachvili, *Intermolecular and surface forces*, University of California, California, 2011.
32 J. Liu, P. K. Thallapally and D. Strachan, *Langmuir*, 2012, **28**, 11584–11589.
33 J. J. Perry, S. L. Teich-McGoldrick, S. T. Meek, J. A. Greathouse, M. Haranczyk and M. D. Allendorf, *J. Phys. Chem. C*, 2014, **118**, 11685–11698.

34 Z. T. Yan, Y. J. Gong, B. H. Chen, X. N. Wu, Q. Liu, L. Cui, S. S. Xiong and S. M. Peng, *Sep. Purif. Technol.*, 2020, **239**, 116514.

35 G. L. Smith, J. E. Eyley, X. Han, X. R. Zhang, J. N. Li, N. M. Jacques, H. G. W. Godfrey, S. P. Argent, L. J. M. McPherson, S. J. Teat, Y. Q. Cheng, M. D. Frogley, G. Cinque, S. J. Day, C. C. Tang, T. L. Easun, S. Rudić, A. J. Ramirez-Cuesta, S. H. Yang and M. Schröder, *Nat. Mater.*, 2019, **18**, 1358–1365.

36 X. F. Wei, J. Miao and L. L. Shi, *Synth. React. Inorg., Met.-Org., Nano-Met. Chem.*, 2016, **46**, 365–369.

37 J. B. Lin, T. T. T. Nguyen, R. Vaidhyanathan, J. Burner, J. M. Taylor, H. Durekova, F. Akhtar, R. K. Mah, O. Ghaffari-Nik, S. Marx, N. Fylstra, S. S. Iremonger, K. W. Dawson, P. Sarkar, P. Hovington, A. Rajendran, T. K. Woo and G. K. H. Shimizu, *Science*, 2021, **374**, 1464–1469.

38 P. Z. Moghadam, A. Li, S. B. Wiggin, A. Tao, A. G. P. Maloney, P. A. Wood, S. C. Ward and D. Fairen-Jimenez, *Chem. Mater.*, 2017, **29**, 2618–2625.

39 X. W. Liu, Y. Guo, A. D. Tao, M. Fischer, T. J. Sun, P. Z. Moghadam, D. Fairen-Jimenez and S. D. Wang, *Chem. Commun.*, 2017, **53**, 11437–11440.

40 L. Deliere, S. Topin, B. Coasne, J. Fontaine, S. D. Vito, C. D. Auwer, P. L. Solari, C. Daniel and Y. Schuurman, *J. Phys. Chem. C*, 2014, **118**, 25032–25040.